IEEE Access
Multidisciplinary ⋮ Rapid Review ⋮ Open Access Journal

Received 13 November 2023, accepted 9 December 2023, date of publication 13 December 2023,
date of current version 18 December 2023.

Digital Object Identifier 10.1109/ACCESS.2023.3342181

RESEARCH ARTICLE

3-D Printed Lattice Core for Wide Angle Scanning Radome at X-Band

DAEYEONG YOON[1], (Graduate Student Member, IEEE), DONG-YEOP NA[2], (Member, IEEE), AND YONG BAE PARK[1,3], (Senior Member, IEEE)

[1]Department of AI Convergence Network, Ajou University, Suwon, Gyeonggi-do 16499, South Korea
[2]Department of Electrical Engineering, Pohang University of Science and Technology, Pohang 37673, South Korea
[3]Department of Electrical and Computer Engineering, Ajou University, Suwon, Gyeonggi-do 16499, South Korea

Corresponding author: Yong Bae Park (yong@ajou.ac.kr)

This work was supported by Korea Electric Power Corporation under Grant R21XO01-12.

ABSTRACT In this paper, we introduce a 3-D printed lattice core for wide-angle scanning radome operating in the X-band. We explain the fundamental design methodology of the sandwich structure for radome and outline the technique to represent the 3-D printed core in terms of its effective dielectric constant. Our study further delve into the electrical characteristics of the unit cell, focusing on its performance with varying incident angles within the X-band. Utilizing 3-D printing technology, we fabricate the sandwich structure and measure its transmittance through the free-space measurement method. Our designed structure achieve a transmittance exceeding 77% for incident angles up to 45 degrees. We fabricate and measure six distinct samples, and the compiled data is present in a table. The findings highlight the high electrical performance of the sandwich structure and demonstrate its suitability for X-band wide-angle scanning applications.

INDEX TERMS Radome, 3-D printer, lattice, periodic structure, wide angle scanning.

I. INTRODUCTION

Aradome is a critical component of antenna systems, protecting antennas from environmental factors such as wind, rain, and temperature changes. Radomes are used in various military and civilian applications, including aircraft, satellites, and ground-based communication systems, and their materials and structures vary depending on the environment [1], [2]. However, the use of radomes can negatively impact electrical characteristics, leading to increased transmission loss and reduced signal quality, especially at higher angles of incidence.

To improve transmission efficiency, various methods such as impedance matching and sandwich structure have been proposed. Impedance matching can minimize reflection by arranging multiple layers of a medium with a lower impedance than the core [3]. However, finding a medium with permittivity intermediate between the core and free space is challenging, so broadband and wide-angle characteristics are often achieved through etching or pyramid-like structures [4], [5], [6]. Unfortunately, uneven surfaces are prone to dust and water build-up. This can cause a rapid deterioration in electrical characteristics, which can be problematic in certain environments [7].

Alternatively, radomes that use multiple composite materials, such as skin, foam, or a honeycomb core, can provide a smooth outer surface. These radomes are lightweight, maintain mechanical properties, and can act as a filter by inserting an FSS layer, making them widely used in defense and aerospace applications [8], [9], [10], [11]. However, the complexity of the manufacturing method and high unit costs hinder the wider use of composite material-based radomes.

3-D printing technology offers a solution to the challenges posed by intricate manufacturing processes. Extensive research in the RF and microwave domains has leveraged the manufacturing flexibility provided by this technology. Specifically, 3-D printing has been utilized to fabricate lens antennas, metasurfaces, and frequency-selective surfaces due to its capability to effortlessly modify effective dielectric constants [12], [13], [14], [15], [16], [17], [18]. When designed

The associate editor coordinating the review of this manuscript and approving it for publication was Photos Vryonides.

meticulously, this periodic structure can enhance mechanical performance. Lattice cores typically offer advantages such as reduced material consumption, lightweight design, and superior mechanical attributes [19], [20], [21], [22]. This structure is well-suited for radomes, where mechanical robustness is of utmost importance. This structure also allows

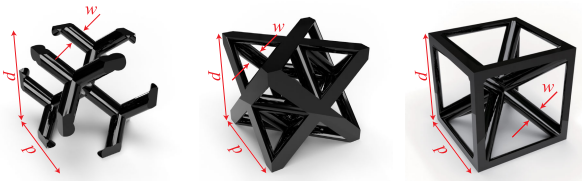

FIGURE 1. Lattice core used for analysis (a) Diamond (b) Octet (c) Star.

the design of advanced radome structures that maintain high transmission over wide angles using the effective dielectric constant. Despite this potential, there is no research yet on radomes utilizing lattice structures for high-angle incident transmission characteristics.

In this paper, we propose a 3-D printed lattice core for wide-angle scanning radomes at X-band, which also offer high-angle incident transmission. We leverage the benefits of 3-D printing technology combined with existing radome structures to enhance their electrical properties. In section II, we analyze the electrical properties of the 3-D printed lattice core. We then design a radome using a lattice core and examine the factors that affect its performance. In section III, we fabricate six structures using a 3-D printer and measure them using the free-space measurement method. In section IV, we compare our results with those from other research studies and discuss our findings. Finally, in section V, we conclude and summarize our study's findings.

II. LATTICE CORE ANALYSIS

A. LATTICE CORE

The lattice core can be made into different shapes like diamond, octet-truss (also called octet), and star. Each shape has branches with a diameter of w and a periodicity of p. This configuration is shown in Fig. 1. Each shape has its own special mechanical characteristics, and these features can be made better if the lattice core is selected and manufactured in the right way. A research by [19] investigated the mechanical properties of 10 different lattice designs. These studies showed that the star and diamond lattice can handle the most weight when bent. Also, they has great strength under bending loading and compression. However, diamond lattice has low energy absorption, mainly due to limited displacement. The octet structure is ideal for scenarios where slight deflection is acceptable but extreme strength is not important. Different lattice cores can be selected based on the varying requirements of the radome's operational environment. This paper focuses on analyzing the electrical characteristics of the three main structures above.

B. EFFECTIVE PERMITTIVITY

Using the Floquet theory in CST Studio Suite [23], we conducted an analysis that considered the periodic structure of the lattice core within the radome. We computed the S-parameters by positioning a Floquet port in both the +z and −z directions and periodic boundary condition. By using

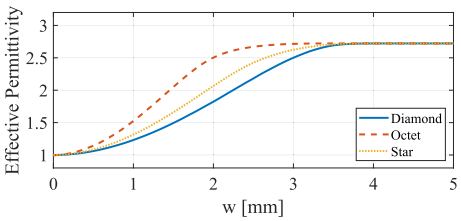

FIGURE 2. Effective permittivity change according to the change of parameter w.

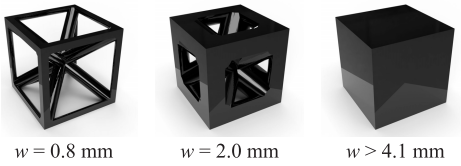

FIGURE 3. The star unit cell changes according to variations in the parameter w, with other structures also transforming into a cube as the value of w increases substantially.

the S-parameters obtained, the effective permittivity can be calculated using the robust method [24], [25]. The scattering parameter has the following relationship with the complex refractive index n and the complex impedance z.

$$S_{11} = \frac{R_{01}(1 - e^{j2nk_0d})}{1 - R_{01}^2 e^{j2nk_0d}}$$
$$S_{21} = \frac{(1 - R_{01})e^{j2nk_0d}}{1 - R_{01}^2 e^{j2nk_0d}} \quad (1)$$

where R_{01} is $z-1/z+1$, k_0 is the free-space wavenumber, and d is the thickness of the medium. The complex impedance z can be expressed by

$$z = \pm\sqrt{\frac{(1 + S_{11})^2 - S_{21}^2}{(1 - S_{11})^2 - S_{21}^2}} \quad (2)$$

$$e^{jnk_0d} = \frac{S_{21}}{1 - S_{11}R_{01}} \quad (3)$$

where the sign of impedance z must satisfy the condition $|e^{jnk_0d} \leq 1|$. Then, taking the logarithm of eqs. (3), the complex refractive index n is defined as below with branch point m.

$$n = \frac{1}{k_0d}\left(\Im\left(\ln e^{jnk_0d}\right) + 2m\pi - j\Re\left(\ln e^{jnk_0d}\right)\right) \quad (4)$$

To calculate the branch point, the Kramer-Kronig relationship can be used [25]. Finally, the effective permittivity ϵ_{eff} and effective magnetic permeability μ_{eff} can be calculated by [24], [25]

$$\epsilon_{eff} = \frac{n}{z}, \quad \mu_{eff} = nz \quad (5)$$

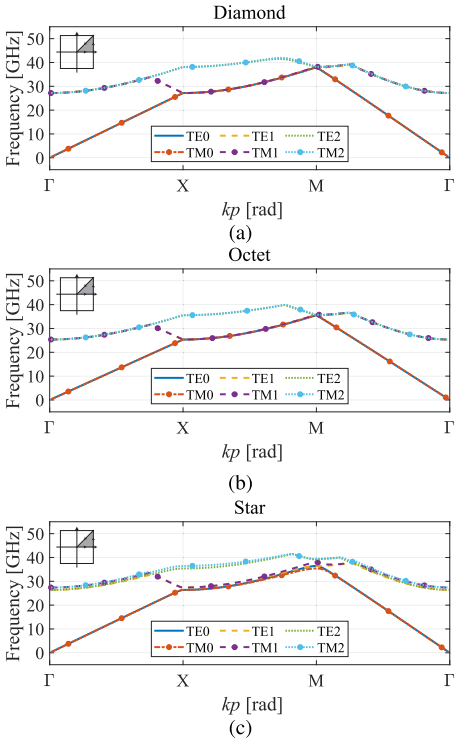

FIGURE 4. Dispersion diagram of lattice core (a) Diamond (b) Octet (c) Star.

The effective permittivity was studied by adjusting the diameter w of the lattice core, with the frequency fixed at 10 GHz. In Fig. 2, as the diameter w increases, both the volume of the grid and the effective dielectric constant increase. However, a critical point is reached when the diameter w increases to the point where the grid volume exceeds the unit cell volume, as shown in Fig. 3. Beyond this threshold, the effective dielectric constant becomes the same as the dielectric constant of the medium being analyzed. In this study, the medium is Formlab's Tough 2000, which has a dielectric constant of 2.72.

C. EIGENMODE ANALYSIS

A dispersion diagram shows the relationship between the propagation constant and frequency [3], [26]. This diagram is essential for accurately identifying the phase and group velocity characteristics of a periodic structure. Moreover, it aids in the identification of permissible modes, thereby clarifying the operational range of the structure.

To construct a dispersion diagram, an eigenmode analysis is executed, taking the Brillouin zone into account. The central point of the Brillouin zone is referred to as the Γ point. Meanwhile, the midpoint of an edge and a face are termed the M and X points, respectively. The interrelationship between these points, periodicity p, and the wave vector is defined by [26]

$$\begin{aligned} \Gamma &= (k_x p = 0,\ k_y p = 0) \\ X &= (k_x p = \pi,\ k_y p = 0) \\ M &= (k_x p = \pi,\ k_y p = \pi) \end{aligned} \tag{6}$$

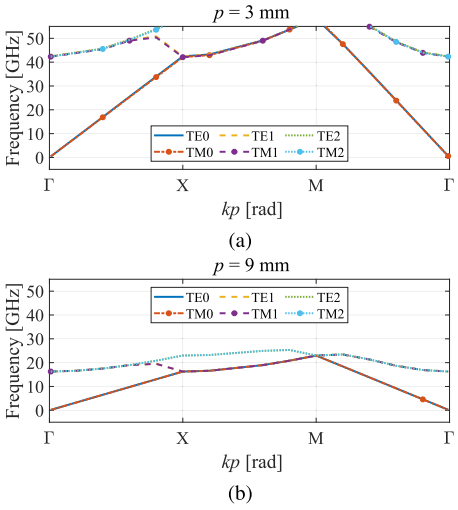

FIGURE 5. Dispersion diagram of Diamond lattice core (a) $p = 3$ mm (b) $p = 9$ mm.

As illustrated in Fig. 4, the dispersion diagram from the eigenmode assessment of the lattice structure shows that, within the X-band—our target frequency range—both TE0 (transverse electric) and TM0 (transverse magnetic) modes are dominant in all three structures. Interestingly, higher-order modes are discernible at the Γ point, occurring at frequencies of 27.1 GHz, 25.4 GHz, and 26.4 GHz for the diamond, octet, and star lattice structures, respectively. These higher-order modes, often referred to as diffraction gratings [27], cause electromagnetic waves to scatter in various directions. Their effect is known to depend on the angle of incidence and the periodicity. Consequently, when frequencies exceed these values, the structure may no longer function effectively as a radome due to the multidirectional scattering. A potential solution to this issue could be reducing the size of the periodic structure, which may extend the operating frequency range [27].

The eigenmode analysis was conducted on a diamond lattice with periodicities p set at 3 mm and 9 mm, respectively, in Fig. 5. For a periodicity p of 3 mm, the higher order mode occurs at 43.9 GHz. When the periodicity p is increased to 9 mm, the higher order mode shifts to 16.3 GHz. This shows the importance of choosing a periodic structure size appropriate for the operating frequency.

III. SANDWICH STRUCTURE ANALYSIS

The proposed lattice core offers the advantage of a customizable effective dielectric constant. This feature has applications beyond lens antennas, notably in radomes that require high angles of incidence. In this chapter, a discussion and analysis of sandwich structures used in radomes is performed.

A. SANDWICH RADOME

In Fig. 6, a composite radome is depicted with a layered configuration, often referred to as a sandwich structure. According to studies [1], [2], sandwich structures can be

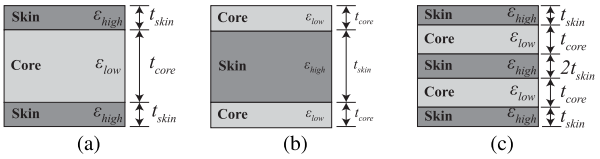

FIGURE 6. 2-D cross-sectional view of sandwich structure. The sandwich structure is classified into A, B, and C types based on the layers of skin and core. (a) A-type (b) B-type (c) C-type.

divided into three distinct types based on their structural layers: Types A, B, and C.

Monolayer structures typically possess a thickness equivalent to half the wavelength. However, this design presents limitations in terms of bandwidth and angle of incidence. To circumvent these limitations, various alternative configurations have been proposed. For instance, A-sandwich structures tackle these problems by employing skins of high permittivity on both the top and bottom, sandwiching a core or foam of lower permittivity in between. The B-sandwich, conversely, feature a high-permittivity material at the center with quarter-wavelength matching layers positioned above and below. Meanwhile, a C-sandwich structure is essentially composed of two A-sandwich layers stacked together, allowing for transmission at higher angles of incidence compared to a single A-sandwich [2].

In this study, we focused on analyzing the A and C-sandwich structures. The skin and core of types A and C are made of a single material and can be fabricated with a 3-D printer. Although the B-sandwich structure, with its low-permittivity lattice core, is a preferred choice, we chose not to include it. This was mainly because the irregularities on its surface render it susceptible to adverse external conditions.

B. PERFORMANCE ANALYSIS

The performance analysis process was described to showcase the excellent characteristics of the proposed structure at high angles of incidence. As a comprehensive analysis of all patterns would be excessively lengthy, we focused on the A-type diamond lattice structure. We examined changes in reflection and transmittance by altering the thickness (t_{skin}), size (p) of the skin (outer surface) and core (which is the diamond lattice) of the A-type structure. The results are displayed in Fig. 7. By default, the design values are $t_{skin} = 0.5$ mm and $p = 5$ mm. As the skin becomes thinner, and the core thicker within the analyzed range, transmittance increases at higher incident angles. The optimal dimensions are 0.3 mm for skin thickness and 9 to 11 mm for the core. However, the optimal skin thickness might not be feasible for printing output. As a result, we chose a thickness of 0.5 mm, which lies within the manufacturable range. Increasing the core size excessively may introduce unwanted modes, potentially affecting performance. However, a size of 5 mm was chosen to ensure stability during the manufacturing process. In addition, since the optimal results from simulations were significant, a C-type sandwich structure was proposed to balance between output stability

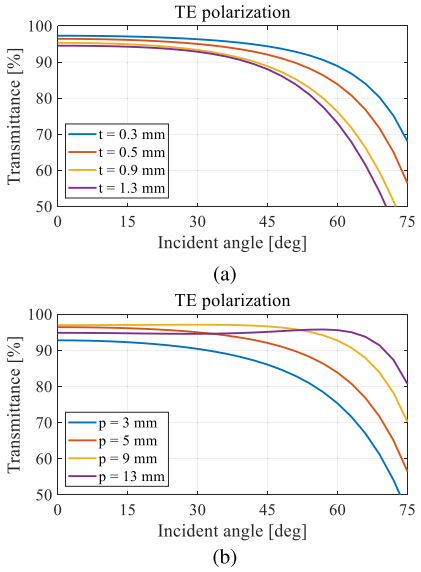

FIGURE 7. Transmittance according to change in incident angle of A-type diamond structure (a) Change in thickness of skin (b) Change in thickness of core.

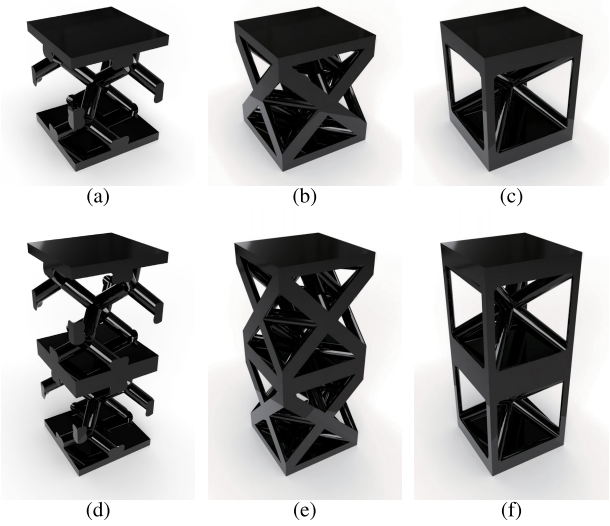

FIGURE 8. Rendered image of lattice core unit cell used for analysis (a, b, c) A sandwich with diamond, octet, and star lattice core (d, e, f) C sandwich with diamond, octet, and star lattice core.

and optimal performance. Simulations for each structure were conducted in the following subsection, and the results were then compared.

C. SIMULATION RESULTS

In our study, we examined the electrical attributes of the sandwich structure intended for radome applications. The key performance indicators in this context are the magnitude and phase of both the reflection and transmission coefficients. Ideally, for optimal performance, the reflectance should remain low while ensuring high transmittance. This minimizes interference with the internal antenna's functionality [1], [2]. The phase of transmission can have significant implications on boresight error (BSE) in practical radome

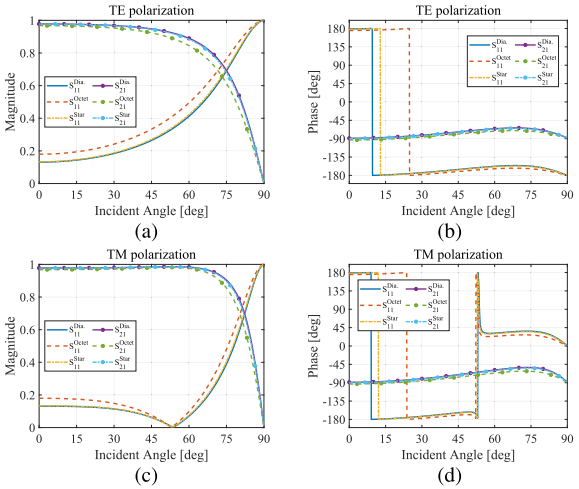

FIGURE 9. Reflection and transmission coefficients of A-sandwich versus incident angle changes at 10 GHz for the proposed lattice core (a, b) Magnitude and phase in TE polarization (c, d) Magnitude and phase in TM polarization.

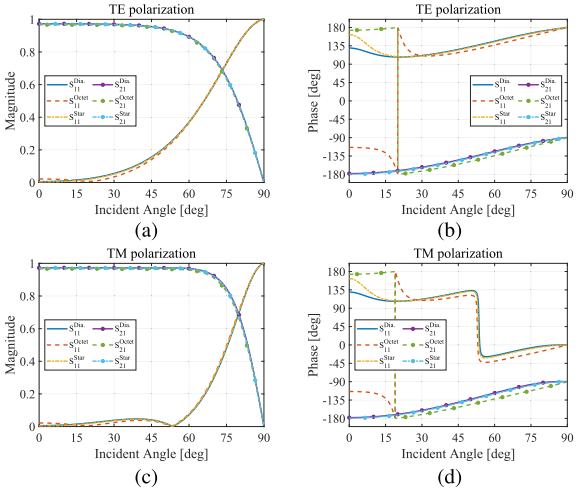

FIGURE 10. Reflection and transmission coefficients of C-sandwich versus incident angle changes at 10 GHz for the proposed lattice core (a, b) Magnitude and phase in TE polarization (c, d) Magnitude and phase in TM polarization.

applications. However, given that BSE can be heavily influenced by the actual shape of the radome [28], such metrics serve more as a reference than an absolute measure.

We have outlined the specifications for the proposed sandwich-type design. The thickness of the skin t_{skin} is 0.5 mm, which is the minimum thickness required for printing stability. Generally, in sandwich structures, the matching characteristics tend to be excellent when the skin thickness is minimal [1], [2]. Each lattice core has the diameter (w) of 0.8 mm and a periodicity (p) of 5 mm. According to Fig. 6, the total thickness of the A-sandwich is 6 mm (with $t_{skin} = 0.5$ mm and $t_{core} = p = 5$ mm). The total thickness of the C-sandwich is 12 mm The dielectric constants for diamond, octet, and star are 1.15, 1.35, and 1.21, respectively. As previously emphasized, the design uses a single medium, which facilitates compatibility with 3-D printing processes, as depicted in Fig. 8.

Figs. 9 and 10 present the reflection and transmission coefficients for the A- and C-type sandwich structures with lattice cores at 10 GHz. In the analysis of each lattice structure, based on incident angle changes, the A-type with octet lattices, particularly in TE polarization, exhibited higher reflectance and lower transmission compared to the diamond and star structures. This indicates that structures with a reduced effective permittivity offer benefits for radome designs. Additionally, the TE polarized light transmission in the A-type structure undergoes a phase shift of up to 25 degrees due to changes in the angle of incidence (See Fig. 9b). As for the reflection coefficient at TM polarization, Figs. 9c and 9d show that a resonance point is formed at 53 degrees. Owing to the reflection coefficient formed at a high angle of incidence, this structure demonstrates high transmittance at high angles of incidence compared to TE polarization.

As shown in Fig. 10a, the C sandwich structure, particularly in its octet, also exhibits higher reflectance compared to its diamond and star. As depicted in Figs. 10b and 10d, the maximum and minimum transmission phases of the C sandwich structure have values of 96 degrees for the octet structure and about 89 degrees for the diamond and star structures. Compared to Type A, Type C exhibits slightly higher losses due to its thicker structure. This is because it demonstrates lower reflectance at high angles of incidence compared to Type A. Hence, by applying a medium with low electrical loss, the performance of Type C can be further enhanced.

D. TOLERANCE ANALYSIS

During the manufacturing process using a 3-D printer, errors may arise based on the machine's precision. In our study, we utilized the Formlabs Form 3+ 3-D printer [29] with the Tough 2000 at 100 μm resolution. Consequently, our tolerance analysis takes into account a 100 μm variation in both the skin thickness (t) and the grid branch thickness (w). Additionally, we analyzed the rate of change based on dielectric constant estimation. The relative dielectric constant of the medium was set at 2.72, with a change rate of 0.072. The loss potential was defined as 0.036, and its change rate was set at 0.008, values derived from errors observed during the measurement process. For tolerance analysis, the sum-root-of-squares model is appropriate, and its equation is defined as

$$\Delta|X| = \sqrt{\Delta|X|_w^2 + \Delta|X|_t^2 + \Delta|X|_{\epsilon_r}^2 + \Delta|X|_{\tan\delta}^2} \quad (7)$$

where X represents reflectance (R) or transmittance (T). Each term can be defined as

$$\Delta|X|_w = \sum \frac{\partial X}{\partial w}\Delta w$$

$$\Delta|X|_t = \sum \frac{\partial X}{\partial t}\Delta t$$

$$\Delta|X|_{\epsilon_r} = \sum \frac{\partial X}{\partial \epsilon_r}\Delta \epsilon_r$$

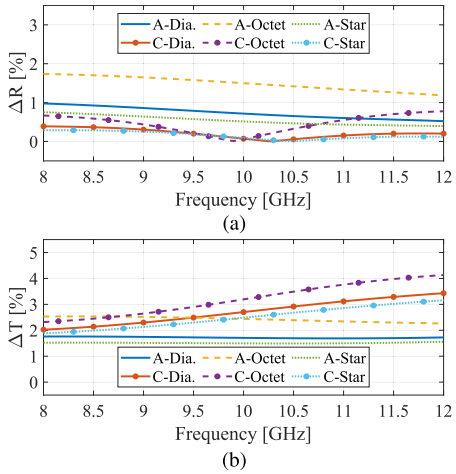

FIGURE 11. Changes in reflectance and transmittance due to manufacturing errors (a) Reflectance (b) Transmittance.

$$\Delta|X|_{\tan\delta} = \sum \frac{\partial X}{\partial \tan\delta} \Delta \tan\delta \tag{8}$$

Transmittance and reflectance variations were analyzed according to frequency under conditions of normal incidence and TE polarization, with the results shown in Fig. 11.

The diamond, octet, and star structures of the A-sandwich exhibit maximum reflectance changes of 0.98%, 1.73%, and 0.75%, and maximum transmittance changes of 1.72%, 2.53%, and 1.55%, respectively. Conversely, for the diamond, octet, and star structures of the C-sandwich, the maximum reflectance changes are 0.39%, 0.77%, and 0.29%, while the maximum transmittance changes are 3.43%, 4.13%, and 3.16%, respectively. The C-sandwich demonstrates a larger variation in maximum transmittance compared to the A-sandwich. This larger variation in maximum transmittance for the C-sandwich can be attributed to its structure, which comprises two A-sandwich layers, potentially increasing tolerance during the manufacturing process. On the other hand, the C-sandwich structure has a lower reflectance than the A-sandwich structure, so the changes in reflectance are relatively minor.

IV. FABRICATION AND MEASUREMENT

A. FABRICATION PROCESS

We used the Form 3+ from Formlabs, a stereolithography (SLA) type 3-D printer [29]. SLA 3-D printers create objects by curing liquid photopolymer resin layer by layer. Given their high-resolution capabilities compared to other methods, they are ideal for producing the proposed structures. To begin, import the modeled 3-D CAD file for printing, create supports, and then send the job to the printer. Once the printing is complete, separate the part from the build platform. Next, clean any remaining resin using isopropyl alcohol and remove the supports. Ultraviolet (UV) curing is then performed to achieve the mechanical properties specified by the manufacturer. However, if UV curing is conducted at high temperatures, the output may be compromised due to excessive heat. To minimize distortion, we chose low-heat curing and extended the curing time. Sandwich samples with the proposed six structures were fabricated, as depicted in Fig. 12. Even with curing at a low temperature, some samples appear slightly bent as seen in Fig. 12b. These geometric distortions might influence reflectance and transmittance.

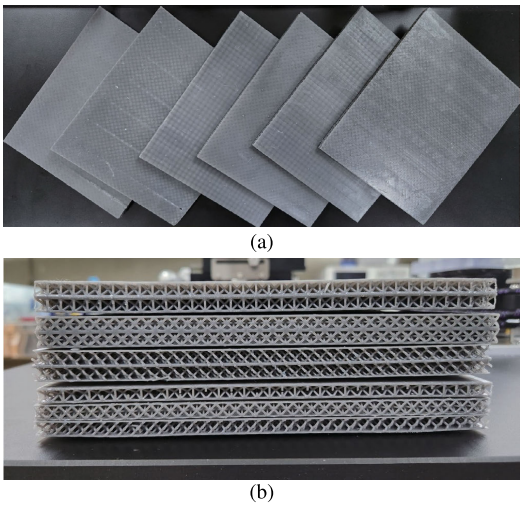

FIGURE 12. Sample fabricated using a 3-D printer (a) sandwich samples (b) cross section view of sandwich samples.

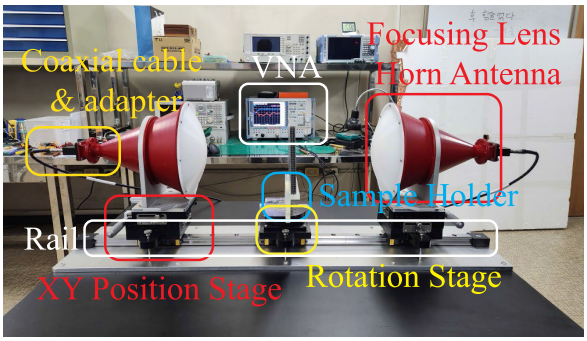

FIGURE 13. Configuration of free-space measurement system.

B. FREE-SPACE MEASUREMENT SYSTEM

To assess the reflection and transmission coefficients of our fabricated structure, we constructed a free-space measurement system, as shown in Fig. 13. We utilized Anteral's focusing lens horn antenna (LHA-F-WR90) to minimize interference from surrounding objects. The two antennas are mounted on a rail, allowing the distance between the sample and the antenna to be adjustable. For precise antenna movement, we installed an XY position stage. The distance between the antenna and the sample holder was set to the focal length. Additionally, a rotation stage was attached to the sample holder to vary the incident angle. The system is equipped with a coaxial cable and adapter to connect the antenna to the vector network analyzer (VNA).

After completing the hardware configuration mentioned above, we employed the method proposed by [30] and [31] to calculate the sample-specific scattering parameters. First,

we performed a 2-port calibration after connecting the cable to the VNA. We then obtained the scattering parameters for an empty sample holder (AIR), assumed to be a perfect electric conductor (PEC), and for the device under test (DUT). Here, the DUT features diamond, octet, and star structures with A- and C- types. To elaborate further, the AIR and PEC signals were initially acquired in the case of normal incidence. Subsequently, the DUT was measured at normal incidence. Following that, the signal was captured by adjusting the angle of the sample holder. All six samples were measured using the process described above. Next, we converted the acquired signal to the time domain using an inverse fast Fourier transform (IFFT) on a computer. By analyzing the S_{11}^{PEC} and S_{11}^{AIR} signals in the time domain, we identified the region of the signal reflected by the sample holder. After defining a window function for the determined time range, we transformed it back into the frequency domain using a fast Fourier transform (FFT). We then convolved the converted window function with the signal obtained from the VNA. This process is also known as the time-gating technique. Finally, we calculated the scattering parameters of the DUT using the method outlined by [30]

$$S_{11}^{MEA.} = \frac{S_{11}^{DUT} - S_{11}^{AIR}}{S_{11}^{AIR} - S_{11}^{PEC}} e^{-2j\beta_0 t_{PEC}}$$
$$S_{21}^{MEA.} = \frac{S_{21}^{DUT} - S_{21}^{PEC}}{S_{21}^{AIR} - S_{21}^{PEC}} e^{j\beta_0 t_{DUT}} \quad (9)$$

where t_{PEC} is the thickness of the copper plate and t_{DUT} is the thickness of the DUT. From the measured scattering parameters, the reflectance ($|R|$) and transmittance ($|T|$) are defined by

$$|R| = |S_{11}^{MEA.}|^2, \quad |T| = |S_{21}^{MEA.}|^2 \quad (10)$$

In our system, reflectance and transmittance can be measured for normal incidence. However, due to the configuration of the jig, measuring the reflection coefficient at oblique incidence is challenging. Therefore, in the subsequent section, we will present both the reflectance and transmittance under normal incidence conditions and the transmittance under oblique incidence conditions for our proposed structure.

C. FREE-SPACE MEASUREMENT RESULTS

The reflection and transmission coefficients of the proposed specimens are depicted in Fig. 14. The A-diamond structure demonstrated −16 dB of reflectance with a transmittance of 92%. For the C-diamond structure, the reflectance is less than −22 dB with a transmittance of 90%. The A-octet structure presented a −14 dB reflectance and a transmittance of 89%. The C-octet structure exhibited a reflectance below −18 dB and a transmittance surpassing 86%. Lastly, the A-star and C-star structures exhibit reflectivity values of −15 dB and −22 dB, with transmittance values of 92% and 89%, respectively. Furthermore, there is good agreement with the simulation within the error range.

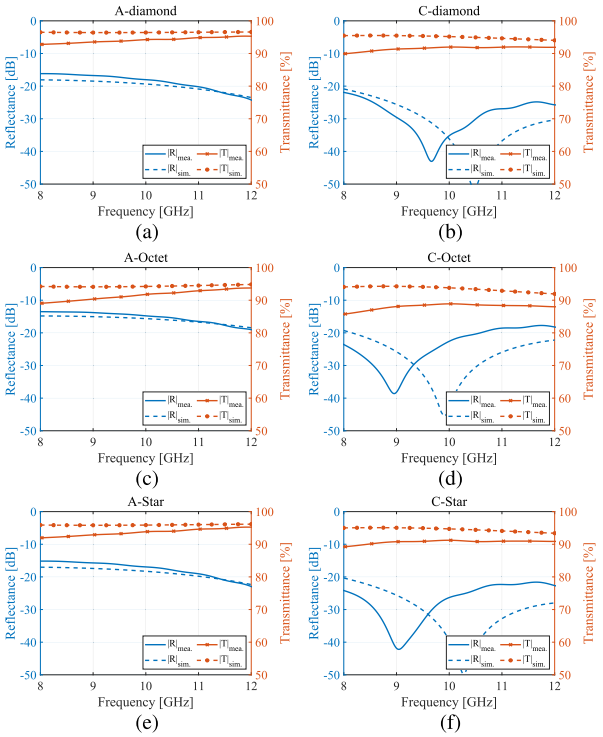

FIGURE 14. Reflectance and transmittance of radome samples at normal incidence (a, b) A-, C-diamond (c, d) A-, C-octet (e, f) A-,C-star.

Measurements were conducted by altering the incident angle from 0 to 45 degrees at X-band, and the results are displayed in Fig. 15. If the manufactured specimen is tilted more than 45 degrees, the effective horizontal size of the specimen becomes $165/\sqrt{2}$ mm, which equals approximately 116.7 mm. Free space measurement using a Gaussian beam is accurate when the size of the specimen is about 3 to 5 times the beam width of the Gaussian beam [32]. However, the size of the specimen is not sufficiently large compared to the −3 dB beam width, which is 34.0 mm on the E-plane and 38.68 mm on the H-plane, respectively, according to the datasheet. Therefore, measurement accuracy cannot be guaranteed at angles beyond 45 degrees; consequently, measurements were performed only up to this angle. The A- and C-diamond structures have a transmittance of 87% and 83% for TE polarization, and over 93% and 90% for TM polarization, respectively. The A-octet structure exhibits an 80% transmittance for TE-polarized waves and 89% or more for TM-polarized waves at 45 degrees or less. The C-octet structure presents a 77% transmittance for TE polarization and 84% or more for TM polarization. Finally, the A-star and C-star structures display transmittance values of 85% and 82% for TE polarization, and 93% and 88% for TM polarization, respectively.

D. RADIATION PATTERN MEASUREMENT RESULTS

To analyze the effect of the radome on radiation patterns, we used a 3-D printed bracket to attach the antenna to the radome. The antenna model used was Eravant's dual ridged

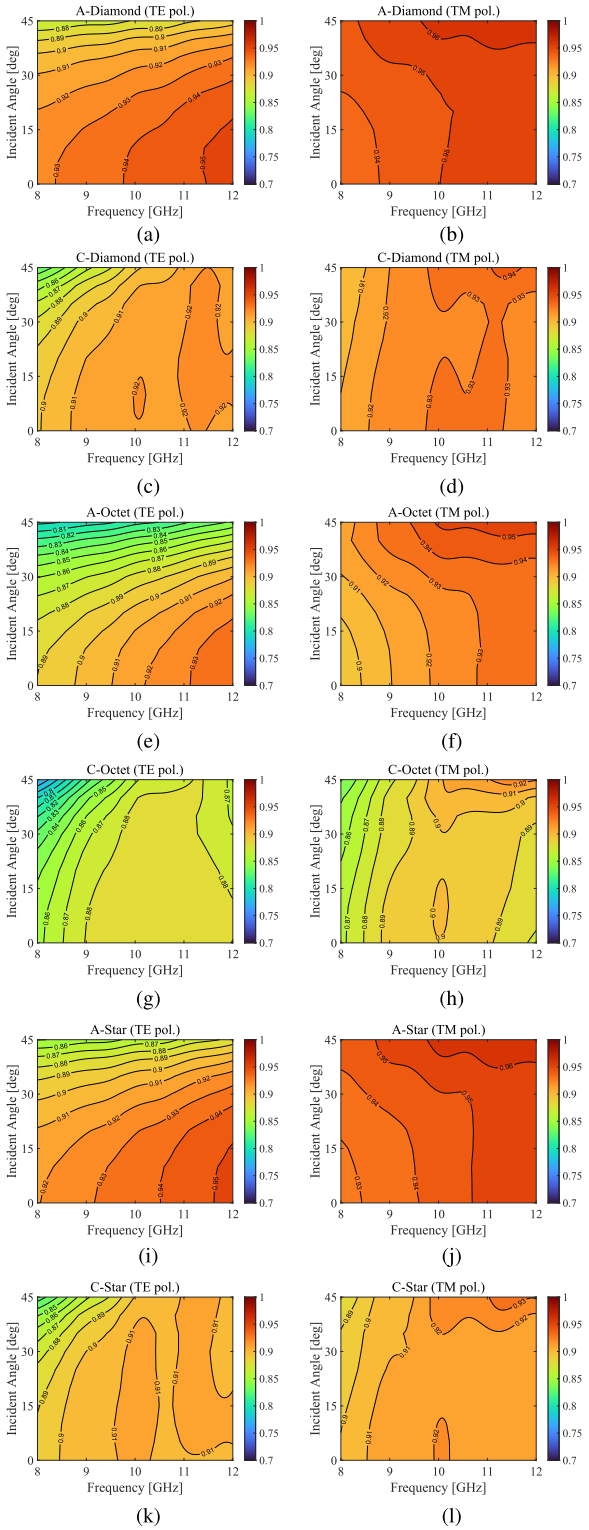

FIGURE 15. TE and TM polarized transmittance of samples in X-band at oblique incidence (a, b) A-diamond (c, d) C-diamond (e, f) A-octet (g, h) C-octet (i, j) A-star (k, l) C-star.

horn antenna (SAV-0636731429-VF-S1), which operates within a 6 to 67 GHz bandwidth.

We measured radiation patterns in the anechoic chamber of the Electromagnetic Wave Technology Institute from the Korea Radio Promotion Association in Seoul. The measurement system, constructed by ORBIT/FR, uses the gain comparison method. These tests compared radiation patterns with and without the radome in place. All six fabricated samples were measured in X-band (8.2 to 12.4 GHz). Since the trends are all similar, the representative results at 10 GHz are shown in Fig. 16.

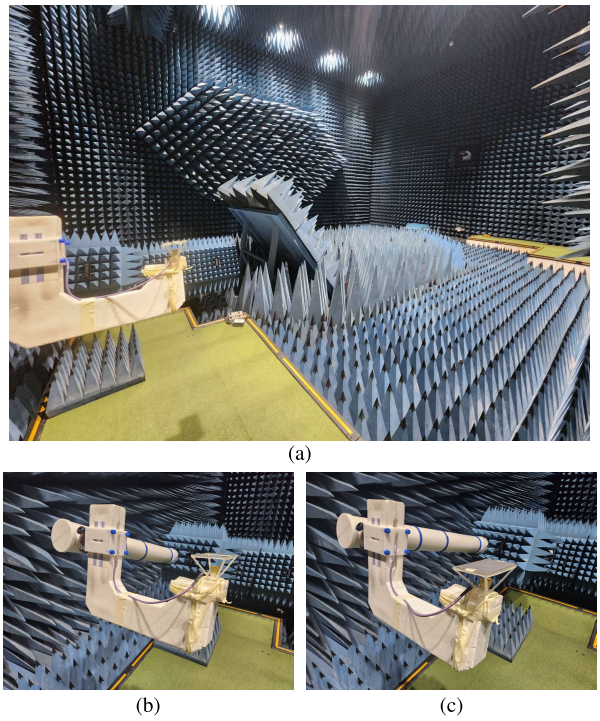

FIGURE 16. Radiation pattern measurement configuration (a) anechoic chamber (b) antenna and radome fixture (c) antenna with radome installed.

Radiation pattern measurements were performed for vertical (V) and horizontal (H) polarizations as shown in Fig. 17. In V polarization, the antenna's peak gain without a radome is observed at 7 degrees, while in H polarization, it peaks at 9 degrees. This is believed to be due to the tilting of the measuring jig or installed fixture. The front aperture patterns (θ in the range of -90 to 90 degrees) show similar trends for both V and H polarizations across all samples. Additionally, a dip occurs at the point where a discontinuity occurs in the radome structure (θ is about $\pm$ 70 degrees). This issue could be resolved by designing the antenna in a completely closed shape. These observations indicate that all six samples can be utilized as radomes. However, there is a noticeable increase in the side lobe level in the posterior region, which is likely attributable to the reflection coefficient of the radome. C-type radomes with low reflectivity exhibit lower side lobe levels compared to A-type, which may explain the observations noted above.

To clearly illustrate the differences between each sample, the peak gain change is presented in Table 1. The peak gain in V polarization occurs at 7 degrees, whereas in H polarization, it occurs at 9 degrees. Additionally, the transmittance at 0 degrees, as estimated by free space

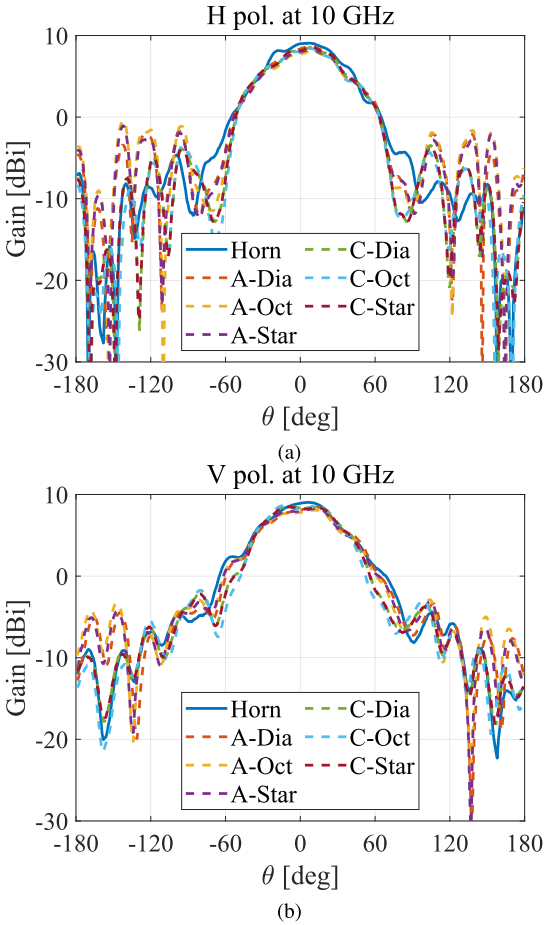

FIGURE 17. Radiation pattern measurement results at 10 GHz (a) vertical Polarization (b) horizontal polarization.

measurement, is provided. The difference between the peak gain change and transmittance is defined and quantified as an absolute error. The magnitude of this absolute error, being up to 0.51 dB, suggests a minimal discrepancy between the two measurement techniques. This represents an error of approximately 12%, attributed to the imprecise manufacturing of the jig. However, the small difference observed between the two measurement systems shows that the radome characteristics can be sufficiently determined with our proposed free space measurement method.

E. DISCUSSION

Table 2 summarizes the measurement results for each sample. Transmittance is categorized by sandwich type and permittivity of the core. The table lists the minimum, mean, and standard deviation values of measurements taken at an incident angle of 45 degrees or less in the X-band. In contrast to TE polarization, TM polarization demonstrates higher transmittance due to the Brewster angle which is apparent at around 50 degrees, as shown in Fig. 9 and Fig. 10. Additionally, sandwiches with a lower permittivity core exhibit higher transmittance. The standard deviation for the C-type sandwich is less than that of the A-type, likely due to the C-type radome's lower reflection coefficient.

TABLE 1. Comparison between two measurement techniques.

Type	A-Diamond	A-Octet	A-Star	C-Diamond	C-Octet	C-Star
Peak Gain Change [dB]	-0.35 (H) -0.64 (V)	-0.95 (H) -1.02 (V)	-0.78 (H) -0.87 (V)	-0.50 (H) -0.64 (V)	-0.66 (H) -0.63 (V)	-0.46 (H) -0.77 (V)
Transmittance [dB]	-0.36	-0.51	-0.36	-0.45	-0.66	-0.51
Absolute Error [dB]	0.01 (H) 0.28 (V)	0.44 (H) 0.51 (V)	0.42 (H) 0.51 (V)	0.05 (H) 0.19 (V)	0.00 (H) 0.03 (V)	0.05 (H) 0.26 (V)

TABLE 2. Summary of measurement results.

Type	Core	ϵ_{low}	Transmittance (%, Meas.)						-3 dB Angle (deg, Sims.)	
			Min		Mean		Std			
			TE	TM	TE	TM	TE	TM	TE	TM
A	Diamond	1.15	87.0	93.4	92.4	95.1	2.07	0.75	75.5	81.9
A	Octet	1.35	79.8	89.4	88.6	92.7	3.53	1.38	71.4	79.3
A	Star	1.21	85.0	92.7	91.6	94.8	2.55	0.93	74.2	81.1
C	Diamond	1.15	83.1	90.0	90.9	92.6	1.60	0.77	72.8	79.8
C	Octet	1.35	76.9	84.0	87.2	89.0	1.97	1.37	69.5	78.4
C	Star	1.21	82.4	88.3	90.3	91.4	1.44	0.81	72.2	79.2

However, despite its lower reflection coefficient, the C-type's transmittance is less than that of the A-type, which suggests that medium loss plays a role.

According to simulated values, Table 2 also provides the angle range where the transmittance is -3 dB or greater. All samples surpass a transmittance of -3 dB at an incident angle of 69 degrees or more. The A-type radome, having relatively low loss, offers a greater transmittance than the C-type. Moreover, a lower permittivity of the inner core corresponds to a broader angle range. This analysis suggests that a more efficient wide-scan radome can be fabricated using a lattice core with both low loss and low effective permittivity.

Comparisons with other studies are showcased in Table 3. Transmittance is documented as a measured value, changing with the incident angle within the given frequency band. However, in the study referenced as [9], the transmittance measurement, which varied with the angle of incidence, was only conducted at 3 GHz. Drawing direct performance comparisons is challenging given the differing results, frequencies, and incident angle conditions across studies.

Yet, for our proposed structure, measurements were conducted at a relatively high incident angle. Notably, the A-diamond boasts an impressive transmittance exceeding 87%. By using materials with low permittivity and loss, even higher transmittance can be anticipated.

TABLE 3. Comparison with other studies.

Reference	Frequency (wavelength)	Type (# of Layers)	Thickness (electrical length)	Material (ϵ_r, tan δ)	Transmittance (Meas.)
[4]	26.5 ~ 40 GHz (11.3 ~ 7.5 mm)	Phyramidal (Graded layer)	4.98 mm (0.55 λ)	Formlab Clear V4 (2.80, 0.032)	Over 77 % ($\theta < 60°$)
[5]	76 ~ 81 GHz (3.94 ~ 3.70 mm)	Phyramidal (Graded layer)	2.9 mm (0.76 λ)	*PEI (3.45, 0.0064)	Over 90 % ($\theta < 35°$)
[7]	3.5 ~ 12.1 GHz (85.7 ~ 24.8 mm)	FSS (5)	4 mm (0.08 λ)	Rogers RT5880 (2.2, 0.001)	Over 50 % ($\theta < 60°$)
[9]	1 ~ 14 GHz (300 ~ 21.4 mm)	5A sandwich (12)	34.8 mm (0.87 λ)	**PTFE (2.2, 0.009) Rogers 4350B (3.48, 0.004) Rohacell 71HF (1.09, 0.0038) Epoxy (2.89, 0.09)	Over 93% ($\theta < 30°$ at 3 GHz)
This Work	8 ~ 12 GHz (37.5 ~ 25 mm)	A-sandwich (3) C-sandwich (5)	6 mm (A, 0.2 λ) 12 mm (C, 0.4 λ)	Formlab Tough 2000 (2.72, 0.036)	Table 1 ($\theta < 45°$)

* PEI: Polyetherimide, **PTFE: Polytetrafluoroethylene

When fabricating a radome with a pyramidal structure, as seen in [4] and [5], there is the benefit of utilizing a singular material. However, the grooved surface might pose challenges in removing foreign substances. Using FSS as in [8] might necessitate metal element processing or layer stacking. Sandwich structures, like in [9], incorporate varied media such as external skin, middle skin, core, and bond-ply, potentially requiring intricate processes to amalgamate them. Conversely, our proposed structure sidesteps issues inherent to the pyramidal shape and doesn't mandate processes like composite fabrication and etching.

V. CONCLUSION

In this paper, we proposed and validated a method for designing wide-angle scanning sandwich structures using additive manufacturing technology. We examined diamond, octet, and star lattice cores and integrated these cores into A- and C-type sandwich structures. The A-diamond, octet, and star structures exhibited transmittance exceeding 80% in the X-band at incident angles of less than 45 degrees. Similarly, the C-diamond, octet, and star structures displayed transmittance of over 77% under the same conditions. Additionally, we estimated the radiation pattern by mounting a radome on each horn antenna, suggesting its suitability for wide-angle scanning applications in the X-band. The proposed analysis method lays the groundwork for future research, aiming to further the creation of more efficient and adaptable radomes for various applications.

REFERENCES

[1] D. J. Kozakoff, *Analysis of Radome-Enclosed Antennas*. Norwood, MA, USA: Artech House, 2010.
[2] R. Shavit, *Radome Electromagnetic Theory and Design*. Hoboken, NJ, USA: Wiley, 2018.
[3] D. M. Pozar, *Microwave Engineering*. Hoboken, NJ, USA: Wiley, 2011.
[4] D. Yoon, D.-Y. Na, and Y. B. Park, "Design and fabrication of tapered dielectric for broadband and wide incident angle transmission," *IEEE Trans. Antennas Propag.*, vol. 70, no. 12, pp. 11922–11933, Dec. 2022.
[5] M. M. S. Hossain, S. A. N. Saqueb, A. H. Arage, J. Cabigao, C. Velasquez, K. Sertel, and N. K. Nahar, "Wideband radomes for millimeter-wave automotive radars," *IEEE Trans. Antennas Propag.*, vol. 70, no. 2, pp. 1178–1186, Feb. 2022.
[6] M. S. Mirotznik, B. L. Good, P. Ransom, D. Wikner, and J. N. Mait, "Broadband antireflective properties of inverse motheye surfaces," *IEEE Trans. Antennas Propag.*, vol. 58, no. 9, pp. 2969–2980, Sep. 2010.
[7] N. Chen, R. Gourova, O. A. Krasnov, and A. Yarovoy, "The influence of the water-covered dielectric radome on 77 GHz automotive radar signals," in *Proc. Eur. Radar Conf. (EURAD)*, Oct. 2017, pp. 139–142.
[8] B. Hua, X. Liu, X. He, and Y. Yang, "Wide-angle frequency selective surface with ultra-wideband response for aircraft stealth designs," *Prog. Electromagn. Res. C*, vol. 77, pp. 167–173, 2017.
[9] Z. Qamar, J. L. Salazar-Cerreno, and N. Aboserwal, "An ultra-wide band radome for high-performance and dual-polarized radar and communication systems," *IEEE Access*, vol. 8, pp. 199369–199381, 2020.
[10] I.-G. Lee, W.-S. Oh, Y. J. Kim, and I.-P. Hong, "Design and fabrication of absorptive/transmissive radome based on lumped elements composed of hybrid composite materials," *IEEE Access*, vol. 8, pp. 129576–129585, 2020.
[11] I. Choi, J. G. Kim, I. S. Seo, and D. G. Lee, "Design of the hybrid composite face with electromagnetic wave transmission characteristics of low-observable radomes," *Compos. Struct.*, vol. 94, no. 11, pp. 3394–3400, Nov. 2012.
[12] S. Zhang, R. K. Arya, S. Pandey, Y. Vardaxoglou, W. Whittow, and R. Mittra, "3D-printed planar graded index lenses," *IET Microw., Antennas Propag.*, vol. 10, no. 13, pp. 1411–1419, Oct. 2016.
[13] C. Wang, J. Wu, and Y.-X. Guo, "A 3-D-printed multibeam dual circularly polarized Luneburg lens antenna based on quasi-icosahedron models for Ka-band wireless applications," *IEEE Trans. Antennas Propag.*, vol. 68, no. 8, pp. 5807–5815, Aug. 2020.
[14] Y.-H. Lou, Y.-X. Zhu, G.-F. Fan, W. Lei, W.-Z. Lu, and X.-C. Wang, "Design of Ku-band flat Luneburg lens using ceramic 3-D printing," *IEEE Antennas Wireless Propag. Lett.*, vol. 20, no. 2, pp. 234–238, Feb. 2021.
[15] R. C. Rumpf, J. Pazos, C. R. Garcia, L. Ochoa, and R. Wicker, "3D printed lattices with spatially variant self-collimation," *Prog. Electromagn. Res.*, vol. 139, pp. 1–14, 2013.
[16] H. Li, G. Wang, G. Hu, T. Cai, C. Qiu, and H. Xu, "3D-printed curved metasurface with multifunctional wavefronts," *Adv. Opt. Mater.*, vol. 8, no. 15, Aug. 2020, Art. no. 2000129.
[17] J. H. Barton, C. R. Garcia, E. A. Berry, R. Salas, and R. C. Rumpf, "3-D printed all-dielectric frequency selective surface with large bandwidth and field of view," *IEEE Trans. Antennas Propag.*, vol. 63, no. 3, pp. 1032–1039, Mar. 2015.
[18] C. R. Garcia, J. Correa, D. Espalin, J. H. Barton, R. C. Rumpf, R. Wicker, and V. Gonzalez, "3D printing of anisotropic metamaterials," *Prog. Electromagn. Res. Lett.*, vol. 34, pp. 75–82, 2012.
[19] S. A. M. Ghannadpour, M. Mahmoudi, and K. H. Nedjad, "Structural behavior of 3D-printed sandwich beams with strut-based lattice core: Experimental and numerical study," *Compos. Struct.*, vol. 281, Feb. 2022, Art. no. 115113.
[20] C. Peng, K. Fox, M. Qian, H. Nguyen-Xuan, and P. Tran, "3D printed sandwich beams with bioinspired cores: Mechanical performance and modelling," *Thin-Walled Struct.*, vol. 161, Apr. 2021, Art. no. 107471.
[21] K. Sugiyama, R. Matsuzaki, M. Ueda, A. Todoroki, and Y. Hirano, "3D printing of composite sandwich structures using continuous carbon fiber and fiber tension," *Compos. A, Appl. Sci. Manuf.*, vol. 113, pp. 114–121, Oct. 2018.
[22] T. Li and L. Wang, "Bending behavior of sandwich composite structures with tunable 3D-printed core materials," *Compos. Struct.*, vol. 175, pp. 46–57, Sep. 2017.
[23] *CST Studio Suite*. Accessed: Dec. 13, 2023. [Online]. Available: https://www.3ds.com/products-services/simulia/products/cst-studio-suite
[24] X. Chen, T. M. Grzegorczyk, B.-I. Wu, J. Pacheco, and J. A. Kong, "Robust method to retrieve the constitutive effective parameters of metamaterials," *Phys. Rev. E, Stat. Phys. Plasmas Fluids Relat. Interdiscip. Top.*, vol. 70, no. 1, Jul. 2004, Art. no. 016608.
[25] Z. Szabó, G.-H. Park, R. Hedge, and E.-P. Li, "A unique extraction of metamaterial parameters based on Kramers–Kronig relationship," *IEEE Trans. Microw. Theory Techn.*, vol. 58, no. 10, pp. 2646–2653, Oct. 2010.
[26] C. A. Balanis, *Advanced Engineering Electromagnetics*. Hoboken, NJ, USA: Wiley, 2012.
[27] E. B. Grann, M. G. Moharam, and D. A. Pommet, "Artificial uniaxial and biaxial dielectrics with use of two-dimensional subwavelength binary gratings," *J. Opt. Soc. Amer. A, Opt. Image Sci.*, vol. 11, no. 10, p. 2695, 1994.

[28] H. Shin, D. Yoon, D.-Y. Na, and Y. B. Park, "Analysis of transmission loss and boresight error of a curved FSS radome-enclosed antenna," *IEEE Access*, vol. 9, pp. 95843–95852, 2021.
[29] *Formlabs Form 3+*. Accessed: Dec. 13, 2023. [Online]. Available: https://formlabs.com/3d-printers/form-3
[30] F. Gonçalves, A. Pinto, R. Mesquita, E. Silva, and A. Brancaccio, "Free-space materials characterization by reflection and transmission measurements using frequency-by-frequency and multi-frequency algorithms," *Electronics*, vol. 7, no. 10, p. 260, Oct. 2018.
[31] G. Dhondt, D. De Zutter, and L. Martens, "An improved free-space technique modelling for measuring dielectric properties of materials," in *Proc. IEEE Antennas Propag. Soc. Int. Symp.*, vol. 1, Jul. 1996, pp. 180–183.
[32] D. Bourreau, A. Peden, and S. Le Maguer, "A quasi-optical free-space measurement setup without time-domain gating for material characterization in the *W*-band," *IEEE Trans. Instrum. Meas.*, vol. 55, no. 6, pp. 2022–2028, Dec. 2006.

DAEYEONG YOON (Graduate Student Member, IEEE) received the B.S. degree in electrical and computer engineering from Ajou University, Suwon, South Korea, in 2018, where he is currently pursuing the integrated M.S./Ph.D. degree in AI convergence network. His research interests include periodic structure, frequency selective surface, radomes, and radar cross section.

DONG-YEOP NA (Member, IEEE) received the B.S. and M.S. degrees in electrical and computer engineering from Ajou University, Suwon, South Korea, in 2012 and 2014, respectively, and the Ph.D. degree in electrical and computer engineering from The Ohio State University, Columbus, OH, USA, in 2018. From 2019 to 2022, he was with the Elmore Family School of Electrical and Computer Engineering, Purdue University, West Lafayette, IN, USA, as a Postdoctoral Research Associate and a Research Scientist. He joined the Department of Electrical Engineering, Pohang University of Science and Technology, Pohang, South Korea, in 2022, where he is currently an Assistant Professor. His research interests include computational electromagnetics, kinetic plasma modeling via particle-in-cell algorithm, and quantum electromagnetics.

YONG BAE PARK (Senior Member, IEEE) received the B.S., M.S., and Ph.D. degrees in electrical engineering from the Korea Advanced Institute of Science and Technology, South Korea, in 1998, 2000, and 2003, respectively. From 2003 to 2006, he was with the Korea Telecom Laboratory, Seoul, South Korea. He joined the School of Electrical and Computer Engineering, Ajou University, South Korea, in 2006, where he is currently a Professor. His research interests include electromagnetic field analysis, high-frequency methods, metamaterial antennas, radomes, and stealth technology.